Modelling Inter and Intra granular Dislocation Transport using Crystal Plasticity FE.

Subhendu Chakraborty [1], Abigail Hunter [2], D.J. Luscher [1]

[1] Theoretical Division, Fluid Dynamics and Solid Mechanics Group, Los Alamos National Laboratory, Los Alamos, NM, USA
[2] X-Computational Physics Division, Materials & Physical Data Group, Los Alamos National Laboratory, Los Alamos, NM, USA
February 13, 2024

Abstract

A dislocation transport based crystal plasticity model is developed.

1 Introduction

Dislocation accommodated plasticity plays an important role in the deformation of most crystalline materials. In metallic materials, movement of dislocations play a critical role in the plastic flow, and accumulation of plastic strain within the material. Due to this, it might be appropriate for any material model at mesoscale to incorporate dislocation transport within grains as well as across grain boundaries for polycrystalline metallic materials.

Development in microscopy technology has provided images which show that the interaction of dislocations with grain boundaries can play a major role in the plastic deformation of metals and the range of viable interactions is more complex than these bounding cases of GBs being fully transparent or opaque to dislocation transfer [1, 2, 3, 4]. These observations motivate the development of a crystal plasticity model that incorporates the physical transport of dislocations both within the grains and across grain boundaries. The model should also incorporate the dependence of dislocation transfer across the GB on the geometric features of grains on either side of a GB, the GB plane, and the local state of material adjacent to the GB, e.g., the resolved shear stress, and dislocation density.

Over the years, many crystal plasticity models are developed to model the plasticity in metallic materials. A detailed overview of such models can be found in [5]. In some of these models, the dislocation transport is incorporated implicitly in the sense that the effect of dislocation movement, i.e. development of plastic strain, is computed either by using a phenomenological shearing rate[6, 7] or by using a model describing the mean dislocation velocity [8, 9]. In these continuum crystal plasticity models dislocations are not physically transported.

On the other hand in a separate class of continuum crystal plasticity theory, the spatial evolution of dislocation density fields represent the consequence of the transport of dislocations throughout the lattice across the material and is a part of the solution variables [10, 11]. In these second class of continuum crystal plasticity material models, the movement of dislocations within the grain is mainly influenced by the resolved shear stress, a relatively long-ranged backstress associated with the polarization of the dislocation density field, and the local hardening of the material due to dislocation reaction and/or dislocation segregation. Across grain boundaries (GBs), it is often assumed that the GB is either completely transparent to a passing dislocation i.e., 100% transfer of dislocations across the GB, or opaque to dislocations, i.e., no transfer across the GB at all.

In [12, 13] the effect of slip transfer across the grain boundary is explored using a density based crystal plasticity model. In this model, the effect of dislocation transfer across the grain boundary is realized by modifying the dislocation source term in the vicinity of the grain boundary that causes the dislocation accumulation near the grain boundary.

In the present work, we build upon the crystal plasticity model that was developed in [10, 11]. This dislocation-density based crystal plasticity model comprises the coupled evolution of three modules:

the Deformation Momentum Balance (DMB), the Continuum Dislocation Transport (CDT), and the Dislocation Deformation Compatibility (DDC). The DMB component of the model describes classical continuum deformation field theory, with the displacement field as the primary unknown variable, and is governed by the principle of conservation of momentum under the applied loading. The CDT component of the model describes the conservation laws for the densities of dislocation populations which are treated as primary field variables. Finally, the DDC sub-problem reconciles evolving dislocation fields from CDT with the deformation and stress fields of DMB. Specifically, solving the DDC sub-problem is necessary to identify the long-range residual stress field, and associated strain field, attributed to the distribution of non-redundant dislocations in the lattice [14, 15, 16]. The previous model considered GBs to be either fully transparent or opaque to the flux of dislocations.

This model was previously published with application to high rate loading conditions [10, 11]. In this previous effort, key advances in the model development included an explicit representation of dislocation transport (CDT), detailed accounting for elastic interactions involving geometrically necessary dislocations (DDC), classical momentum balance (DMB), and the tight coupling between all three of these sub-problems.

Here we present an implementation that can be applied to low rate and quasi-static loading conditions. We use the open-source finite-element library 'Multiphysics Object Oriented Simulation Environment' (MOOSE) [17] as the base code. MOOSE is an open-source finite element framework developed in C++ at Idaho National Laboratory. The modular structure of MOOSE makes it convenient to incorporate new physics including new constitutive theories or additionally coupled partial differential equations within it. The integration of MOOSE with PETSc [18, 19] makes it convenient to leverage various efficient non-linear solvers. The 'DiscoFlux' material model is implemented within the MOOSE framework using a semi-implicit solution strategy for each sub-component. Additionally, we have expanded the CDT sub-problem and solution to account for dislocation transport both within grains and across grain boundaries when modeling polycrystalline materials. To put these advances into context, we first present a brief summary of key equations in the DMB and DDC modules in Sections 2.1 and 2.2. The CDT module is described in more detail in Section 2.3. Simulation results to demonstrate the applicability of this new model are presented for single crystal, bi-crystal and poly-crystal numerical test problems presented in Section 3.

2 Computational methodology

2.1 Deformation Momentum Balance(DMB)

2.1.1 Governing equation

The governing differential equation to model the deformation of a deformable body is obtained by imposing the conservation of linear momentum and can be expressed as,

$$\nabla_{\mathbf{0}} \cdot \mathbf{P} = \rho_0 \, \ddot{\mathbf{x}} \tag{1}$$

where $\mathbf{P}$ is the first Piola-Kirchhoff stress, $\mathbf{x} = \phi(t, \mathbf{X})$ is the deformed position vector of the material point within the body which originally coincided with the position $\mathbf{X}$ of the same material point in the undeformed reference configuration, t is time, and ϕ is the mapping function from the reference configuration to the current, i.e. deformed configuration. ρ_0 is the density of the material in the undeformed configuration. In the present work, we focus on problems with a slow rate of deformation consistent with quasi-static conditions, and therefore omit the inertia term in equation 1 enabling rewriting as

$$\nabla_{\mathbf{0}} \cdot \mathbf{P} = 0 \,. \tag{2}$$

2.1.2 Kinematics

Finite deformation kinematics employed here include deformation modes associated with elastic stretching of the lattice, crystal lattice rotation, and plastic slip. The deformation gradient $\mathbf{F}$ admits a multiplicative decomposition into elastic and plastic components, respectively, i.e.,

$$\mathbf{F} = \mathbf{F}_{\mathrm{e}}\mathbf{F}_{\mathrm{p}} \quad \text{where} \quad \det \mathbf{F}_{\mathrm{e}} > 0 \quad \text{and} \quad \det \mathbf{F}_{\mathrm{p}} = 1 \,. \tag{3}$$

The elastic part of the deformation gradient $\mathbf{F}_{\mathrm{e}}$ incorporates both lattice rotation and elastic stretch through the relation $\mathbf{F}_{\mathrm{e}} = \mathbf{R}_{\mathrm{e}}\mathbf{U}_{\mathrm{e}}$. The rates of the elastic and plastic components of the deformation gradient are given as

$$\dot{\mathbf{F}}_{\mathrm{e}} = \mathbf{L}\mathbf{F}_{\mathrm{e}} - \mathbf{F}_{\mathrm{e}}\mathbf{L}_{\mathrm{p}} \quad \text{and} \quad \dot{\mathbf{F}}_{\mathrm{p}} = \mathbf{L}_{\mathrm{p}}\mathbf{F}_{\mathrm{p}} \,. \tag{4}$$

Variable Name	Definition
$\mathbf{S}$	First Piola-Kirchhoff stress
$\hat{\mathbf{S}}$	Second Piola-Kirchhoff stress
σ	Cauchy stress
ρ_0	Mass density of the material in reference configuration
$\mathbf{F}$	Deformation gradient
$\mathbf{F}_e$	Elastic part of $\mathbf{F}$
$\mathbf{F}_p$	Plastic part of $\mathbf{F}$
$\mathbf{L}$	Velocity gradient
$\mathbf{L}_p$	Plastic part of $\mathbf{L}$
$\dot{\gamma}$	Plastic shearing rate
$\mathbf{s}_0$	Slip direction in reference configuration
$\mathbf{n}_0$	Slip plane normal in reference configuration
$\mathbf{S}_0$	Schmid tensor in reference configuration
$\mathbf{E}_e$	Elastic Green-Lagrange strain
ρ_e^α	Edge dislocation density
ρ_s^α	Screw dislocation density
$\rho_\perp^\alpha$	Edge positive dislocation density
$\rho_\top^\alpha$	Edge negative dislocation density
$\rho_\odot^\alpha$	Screw positive dislocation density
$\rho_\oplus^\alpha$	Screw negative dislocation density
κ^α	GND density
τ^α	Resolved shear stress
τ_b^α	Back stress
τ_{cr}^α	Slip system resistance
$\mathbf{S}_{int}$	Total internal stress due to GNDs
f^α	Dislocation flux across the Grain Boundary
b	Magnitude of burger vector
$\mathbf{v}^\alpha$	Dislocation velocity vector
v_c	Shear wave speed in the material
$\mathbf{I}$	Second order identity tensor
$\times$	Cross product
$\otimes$	Dyadic product
$:$	Inner product

Table 1: A brief definition of all the significant variables used in the work.

where $\mathbf{L} = \dot{\mathbf{F}}\mathbf{F}^{-1}$ and $\mathbf{L}_p = \dot{\mathbf{F}}_p \mathbf{F}_p^{-1}$. For dislocation-mediated plasticity, the plastic part of the velocity gradient $\mathbf{L}_p$ is expressed in terms of a summation of crystallographic slip rates $\dot{\gamma}^\alpha$ on each slip system α as

$$\mathbf{L}_p = \dot{\mathbf{F}}_p \mathbf{F}_p^{-1} = \sum_{\alpha=1}^{N_{slip}} \dot{\gamma}^\alpha \mathbf{s}_0^\alpha \otimes \mathbf{n}_0^\alpha = \sum_{\alpha=1}^{N_{slip}} \dot{\gamma}^\alpha \mathbf{S}_0^\alpha \,. \tag{5}$$

The Schmid tensor is expressed as $\mathbf{S}_0^\alpha \stackrel{\text{def}}{=} \mathbf{s}_0^\alpha \otimes \mathbf{n}_0^\alpha$, where $\mathbf{s}_0^\alpha$ and $\mathbf{n}_0^\alpha$ are respectively the slip direction and slip plane normal as defined in the reference configuration. The face centered cubic (fcc) crystal structure has four slip planes that are represented by slip plane normals $\mathbf{n}_0^\alpha$, with each slip plane having three slip directions represented by $\mathbf{s}_0^\alpha$. N_{slip} is the total number of slip systems which is 12 for fcc materials.

The stress-strain relation is expressed in an elastically undeformed reference configuration, in terms of the second Piola-Kirchhoff stress $\hat{\mathbf{S}}$ and the elastic Green-Lagrange strain $\mathbf{E}_e$,

$$\hat{\mathbf{S}} = \mathbb{C} : \mathbf{E}_e \,, \tag{6}$$

where $\mathbb{C}$ is a fourth-order anisotropic elasticity tensor in the material symmetry coordinates. The second

Piola-Kirchhoff stress $\hat{\mathbf{S}}$ and the elastic component of the Green-Lagrange strain tensor $\mathbf{E}_e$ are respectively defined as,

$$\hat{\mathbf{S}} \equiv det(\mathbf{F}_e)\mathbf{F}_e^{-1}\sigma\mathbf{F}_e^{-T} \text{ and } \mathbf{E}_e \equiv \frac{1}{2}\left(\mathbf{F}_e^{\mathbf{T}}\mathbf{F}_e - \mathbf{I}\right) \tag{7}$$

where $\mathbf{I}$ is the 2nd order identity tensor and σ is the Cauchy stress tensor.

2.1.3 Crystal plasticity material model

For dislocation density-based crystal plasticity material models, the crystallographic slip rate $\dot{\gamma}^{\alpha}$ is calculated from Orowan's equation [20], and can be written as

$$\dot{\gamma}^{\alpha} = \rho_m^{\alpha}bv^{\alpha} \tag{8}$$

where ρ_m^{α} and v^{α} are the mobile dislocation density and dislocation velocity on slip system α, respectively, and b is the magnitude of the Burgers vector. Following [21], the positive and negative character of edge and screw dislocations are tracked as separate dislocation density field variables. Hence, ρ_m^{α} has contributions from both positive and negative edge and screw dislocations, i.e.,

$$\rho_m^{\alpha} = \rho_{m,\perp}^{\alpha} + \rho_{m,\top}^{\alpha} + \rho_{m,\odot}^{\alpha} + \rho_{m,\oplus}^{\alpha} \tag{9}$$

where $\rho_{m,\perp}^{\alpha}$, $\rho_{m,\top}^{\alpha}$, $\rho_{m,\odot}^{\alpha}$ and $\rho_{m,\oplus}^{\alpha}$ are edge-positive, edge-negative, screw-positive and screw-negative mobile dislocation density, respectively. Thus, the total mobile edge dislocation density can be expressed as $\rho_{m,e}^{\alpha} = \rho_{m,\perp}^{\alpha} + \rho_{m,\top}^{\alpha}$ and similarly for screw dislocations $\rho_{m,s}^{\alpha} = \rho_{m,\odot}^{\alpha} + \rho_{m,\oplus}^{\alpha}$. To model the local evolution of the dislocation densities, the substructure evolution of dislocations are separated based on well-known mechanisms of dislocation network evolution. The five key mechanisms are identified as: (i) nucleation of new dislocations, (ii) multiplication of mobile dislocations, (iii) trapping of mobile dislocations rendering them immobile [22], (iv) annihilation of dislocations through interaction with dislocations of the opposite polarity and (v) reduction of immobile dislocation density due to the recovery process. Then the evolution of mobile and immobile dislocation takes the form [9],

$$\dot{\rho}_m^{\alpha} = \dot{\rho}_{nuc}^{\alpha} + \dot{\rho}_{mult}^{\alpha} - \dot{\rho}_{trap}^{\alpha} - \dot{\rho}_{m\text{-ann}}^{\alpha} \tag{10}$$

$$\dot{\rho}_{im}^{\alpha} = \dot{\rho}_{trap}^{\alpha} - \dot{\rho}_{im\text{-ann}}^{\alpha} - \dot{\rho}_{rec}^{\alpha} \tag{11}$$

where the subscripts nuc, mul, trap, ann and rec stands for nucleation, multiplication, trapping, annihilation and recovery, respectively. In the present study, the terms related to nucleation and recovery are omitted. The other terms in the evolution equations 10 and 11 are expressed as

$$\dot{\rho}_{multi}^{\alpha} = \frac{c_{mult}}{b^2}|\dot{\gamma}_p^{\alpha}| \tag{12a}$$

$$\dot{\rho}_{trap}^{\alpha} = \frac{c_{trap}}{b}\sqrt{\rho_f^{\alpha}}|\dot{\gamma}_p^{\alpha}| \tag{12b}$$

$$\dot{\rho}_{m\text{-ann}}^{\alpha} = c_{m\text{-ann}}\rho_m^{\alpha}|\dot{\gamma}_p^{\alpha}| \tag{12c}$$

$$\dot{\rho}_{im\text{-ann}}^{\alpha} = c_{im\text{-ann}}\rho_{im}^{\alpha}|\dot{\gamma}_p^{\alpha}| \tag{12d}$$

where $c_{multi}, c_{trap}, c_{m\text{-ann}}$ and $c_{im\text{-ann}}$ are material parameters. ρ_f^{α} is the forest dislocation density on the αth slip system. ρ_f^{α} is computed from the total dislocation density by projecting the density onto slip system α, and can be expressed as,

$$\rho_f^{\alpha} = \sum_{\beta=1}^{N_{slip}} A_f^{\alpha\beta}\rho^{\beta} \text{ where } A_f^{\alpha\beta} = \frac{1}{2}|\mathbf{n}^{\alpha}.\mathbf{s}^{\beta}| + \frac{1}{2}|\mathbf{n}^{\alpha}.(\mathbf{n}^{\beta}) \times \mathbf{s}^{\beta}|. \tag{13}$$

The geometrically necessary dislocation (GND) [23, 20, 24] densities for edge and screw populations active on the αth slip system are expressed as,

$$\kappa_e^{\alpha} = \rho_{m,\perp}^{\alpha} - \rho_{m,\top}^{\alpha} \tag{14a}$$

$$\kappa_s^{\alpha} = \rho_{m,\odot}^{\alpha} - \rho_{m,\oplus}^{\alpha}, \tag{14b}$$

4

From equations 5 and 8 the evolution of the plastic deformation can be written using the Orowan relation, i.e.,

$$\dot{\mathbf{F}}_p \mathbf{F}_p^{-1} = \sum_{\alpha=1}^{N_{slip}} b^\alpha (\rho_e^\alpha v_e^\alpha + \rho_s^\alpha v_s^\alpha) \mathbf{s}_0^\alpha \otimes \mathbf{n}_0^\alpha \tag{15}$$

where v_e^α and v_s^α are the signed scalar velocity of edge and screw dislocation densities, respectively, on slip system α.

In general, the dislocation velocity can be expressed as,

$$v^\alpha = \hat{v}(\tau^\alpha, \rho^\beta, T), \tag{16}$$

where τ^α is the resolved shear stress on slip system α. The mean velocity of gliding dislocations is expressed as [25, 10],

$$v^\alpha = \frac{\bar{L}}{t_w + t_r} \text{sign}(\tau^\alpha - \tau_b^\alpha), \tag{17}$$

where $\bar{L}$ is the mean spacing between obstacles, t_w is the wait time that a dislocation spends at an obstacle waiting to overcome it, and t_r is the run time for a dislocation to freely glide between two obstacles. Because in the present study the main obstacle for the movement of a dislocation is another (forest) dislocation, $\bar{L}$ is simply approximated as $\bar{L} = 1/\sqrt{\rho}$, where ρ is the total dislocation density on each slip system.

The waiting time, t_w, for a dislocation to overcome an obstacle characterizes a process which is both stress driven as well as thermally activated and can be expressed as [25, 10, 26],

$$t_w = \frac{1}{\omega} \left(\exp\left[\frac{\Delta G(\tau)}{KT} \right] \right), \tag{18}$$

where ω is the attempt frequency, and K is the Boltzman constant. ΔG is the stress-assisted activation energy and is expressed as,

$$\Delta G^\alpha(\tau) = \Delta G_0 \left\langle 1 - \left(\frac{|\tau^\alpha - \tau_b^\alpha|}{\tau_{cr}^\alpha} \right)^{q_1} \right\rangle^{q_2}, \tag{19}$$

where $\langle x \rangle = 1/2(|x| + x)$, ΔG_0 is the thermal activation constant computed as $\Delta G_0 = g_0 \mu b^3$, τ_b^α is the GND induced slip system back stress and τ_{cr}^α is the slip system resistance of slip system α. The exponents q_1 and q_2 are material parameters. The slip resistance, τ_{cr}^α, due to the interaction between a glide dislocation and other dislocations, is expressed in Taylor hardening form as

$$\tau_{cr}^\alpha = \tau_0 + c_1 \mu b \sqrt{\sum_\beta H_{\alpha\beta}(\rho_e^\beta + \rho_s^\beta)}, \tag{20}$$

where τ_0 is the is intrinsic resistance to dislocation glide due to lattice friction, c_1 is a material constant and $H_{\alpha\beta}$ is the interaction matrix for hardening [27]. The back stress τ_b^α is computed from the internal stress ($\mathbf{S}_{int}$, see Section 2.2) as,

$$\tau_b^\alpha = \mathbf{S}_{int} : \mathbf{s}_0^\alpha \otimes \mathbf{n}_0^\alpha. \tag{21}$$

The run time, t_r, is the average free-running time between obstacles and can expressed as,

$$t_r = \frac{\bar{L}}{v_r} \tag{22}$$

where v_r is the running velocity of the dislocation as it glides between two obstacles. The upper limit of free running velocity is restricted to the sound wave speed in that material due to the viscous drag effect. This velocity can be written as [25, 10]

$$v_r^\alpha = c_s(\sqrt{(\xi^\alpha)^2 + 1} - \xi^\alpha), \tag{23}$$

and where ξ^α is expressed as,

$$\xi^\alpha = \frac{B_0(T)c_s}{2b(\tau^\alpha - \tau_b^\alpha)}. \tag{24}$$

Figure 1 shows the variation of the dislocation velocity with respect to three parameters, c_1, q_1 and q_2, in equations 19 and 20. For the calculated velocities plotted in this figure, the back stress, τ_b, is assumed to be zero. Any other parameter not specified is assigned the value shown in Table 2
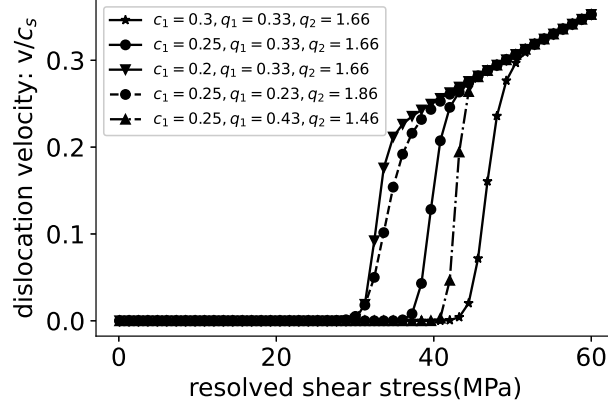
5

Figure 1: Parametric study of dislocation velocity. The parameters explored are: c_1, q_1 and q_2 in equations 19 and 20

.

2.2 Dislocation Deformation Compatibility(DDC)

The evolution of the mobile dislocation density field has a local contribution associated with dislocation network evolution represented by equation 10, and a non-local contribution resulting from transport. Dislocation transport causes a net-polarity of the dislocation density field because under an identical effective resolved shear stress dislocations of opposite polarity will travel in opposite directions. This non-zero net-polarity of the dislocation density field leads to the development of an internal stress field associated with long-range elastic interactions of the dislocations via lattice curvature. This internal stress field can either enhance or impede the further movement of dislocations. In DiscoFlux, this internal stress field is approximated as a simple expression related to the gradient of the GND density at a particular material point. There are several related models that similarly approximate this internal stress field in terms of the GND density [28, 29]. Here we use the expression proposed in [10] according to which the internal stress is computed as

$$\tau_{int}^{\alpha} = \frac{\mu b}{2\pi(1-\nu)} L_0^2 \nabla_s \kappa^{\alpha}(z) \,, \tag{25}$$

where τ_{int}^{α} and κ^{α} are the internal stress and GND density, respectively, on slip system α, μ and ν are the effective isotropic shear modulus and Poisson's ratio of the material, and ∇_s is the directional derivative along the slip direction. The total internal stress is computed as the summation of contributions from each individual slip system, i.e.,

$$\mathbf{S}_{int} = \sum_{\alpha=1}^{N_{slip}} \tau_{int}^{\alpha} \mathbf{M}_0^{\alpha} \,, \tag{26}$$

where $\mathbf{M_0}$ is expressed as,

$$\mathbf{M}_0 = \frac{1}{2}(\mathbf{s_0^{\alpha}} \otimes \mathbf{n_0^{\alpha}} + \mathbf{n_0^{\alpha}} \otimes \mathbf{s_0^{\alpha}}) \,. \tag{27}$$

2.3 Continuum Dislocation Transport(CDT)

During plastic deformation of crystalline solids, the dislocation mediated plastic deformation occurs due to the movement of dislocations. The associated transport of dislocations occurs both within individual grains and also across GBs.

2.3.1 Dislocation transport within the grain

The nonlocal evolution of the dislocations within the grain is modeled using the standard field advection equation. For a conserved scalar quantity, ρ, this can be written as

$$\dot{\rho^{\alpha}} + \nabla_0 \cdot (\rho^{\alpha} \mathbf{v}_c^{\alpha}) = s_{\alpha} \,, \tag{28}$$

where s_{α} is the source term and $\mathbf{v}_c^{\alpha}$ is the dislocation velocity vector on slip system α. The subscript c in the velocity indicates that the dislocation velocity on slip system α depends on the character of the

6

dislocation and can be expressed as

$$\mathbf{v}_\perp^\alpha = v_e^\alpha(\tau^\alpha, \rho_c^\beta, T)\mathbf{s}_0^\alpha$$
$$\mathbf{v}_\top^\alpha = -v_e^\alpha(\tau^\alpha, \rho_c^\beta, T)\mathbf{s}_0^\alpha$$
$$\mathbf{v}_\odot^\alpha = v_s^\alpha(\tau^\alpha, \rho_c^\beta, T)\mathbf{s}_0^\alpha \times \mathbf{n}_0^\alpha \qquad (29)$$
$$\mathbf{v}_\oplus^\alpha = -v_s^\alpha(\tau^\alpha, \rho_c^\beta, T)\mathbf{s}_0^\alpha \times \mathbf{n}_0^\alpha\,.$$

2.3.2   Dislocation transport across the grain boundary

It is generally well understood, and had been directly observed [3, 4], that GBs in a polycrystalline material are a barrier to the free movement of dislocations. Consequently, dislocations typically accumulate or pile up at GBs during plastic deformation processes. However, many GBs allow finite (non-zero) slip transfer across the interface, effectively enabling some dislocation movement through-out the polycrystal. The permeability of dislocations across a GB depends on several different factors related to the GB character and the adjacent material state variables (e.g. stress, dislocation density). There are two main types of criterion that have been used to determine the probability of transfer of dislocation across a GB: geometric criterion [30] and energetic criterion [31]. A detailed review of these approaches can be found in [32, 3, 33]. In the present work, we focus on geometry based criterion, recognizing that the framework will permit future extension to models that capture the evolving description of the GB character in the context of energy and other state descriptors. The rationale behind this choice is that different combinations of multiple geometric features of the GB and the adjacent grains can give rise to a similar GB energy but very different transmission behavior.

Figure 2 shows a typical arrangement of a GB with the relevant geometric features and a single pair of slip systems from the adjacent grains [32].
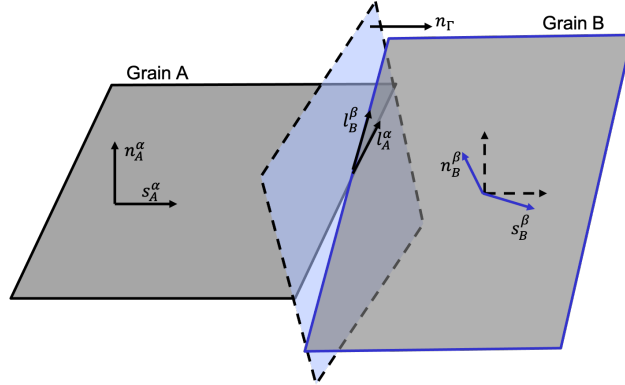

Figure 2: A schematic representation of the relevant geometric features used within the dislocation flux transfer criteria in this work following [32]. Slip plane normal, $\mathbf{n}^\alpha$, and direction, $\mathbf{m}^\alpha$, for a particular pair of slip systems α and β in adjacent Grains A and B, respectively, and the GB interface normal direction, $\mathbf{n}_\Gamma$, are denoted. The intersection of the slip planes and the GB surface are indicated by the vectors $\mathbf{l}$.

In the geometry based criterion, geometric features of the GB and grains, e.g. slip directions $\mathbf{s}_A^\alpha, \mathbf{s}_B^\beta$, slip plane normals $\mathbf{n}_A^\alpha, \mathbf{n}_B^\beta$, and the GB plane normal n_Γ, are used to construct the criterion. Here Grains A and B represent the two grains that are involved in the formation of the GB, n_Γ. There are several geometric criteria that have been developed in the past to model the dislocation transfer across a GB, e.g. in [34] the interaction matrix is defined as

$$N_{\alpha\beta} = (\mathbf{n}_A^\alpha \cdot \mathbf{n}_B^\beta)(\mathbf{s}_A^\alpha \cdot \mathbf{s}_B^\beta) + (\mathbf{n}_A^\alpha \cdot \mathbf{s}_B^\beta)(\mathbf{s}_A^\alpha \cdot \mathbf{n}_B^\beta)\,. \qquad (30)$$

The interaction matrix $N_{\alpha\beta}$ is an $N_{slip} \times N_{slip}$ matrix, where N_{slip} is the number of slip systems in the material. This geometric criterion assumes that the local stress developed in the adjacent grain due to the pile-up of dislocations in the neighboring grain is purely shear in nature. The above criterion is slightly modified by dropping the second term and used in collaboration with the Schmid factor and stress concentration ahead of the pile-up [33] to determine the outgoing slip system when a dislocation

7

transmits across a GB. None of the above criterion consider any features of the GB itself e.g, the GB plane normal. Conversely, other criteria have been proposed that do incorporate some of the GB features, such as that developed in [35, 36],

$$M_{\alpha\beta} = (\mathbf{l}_A^\alpha \cdot \mathbf{l}_B^\beta)(\mathbf{s}_A^\alpha \cdot \mathbf{s}_B^\beta), \tag{31}$$

where $\mathbf{l}_A^\alpha$ is the line of intersection between the GB plane and slip plane α of Grain A defined as $\mathbf{l}_A^\alpha = (\mathbf{n}_A^\alpha \times \mathbf{n}^\Gamma)/|\mathbf{n}_A^\alpha \times \mathbf{n}^\Gamma|$. Here $\mathbf{n}_\Gamma$ is the unit normal vector to the GB. This criterion is used to determine the slip plane of the outgoing dislocation and a separate stress criterion is used to determine the slip direction within that slip plane. Figure 3(a) shows the interaction matrix calculated using equation 31

(a)

(b)

(c)
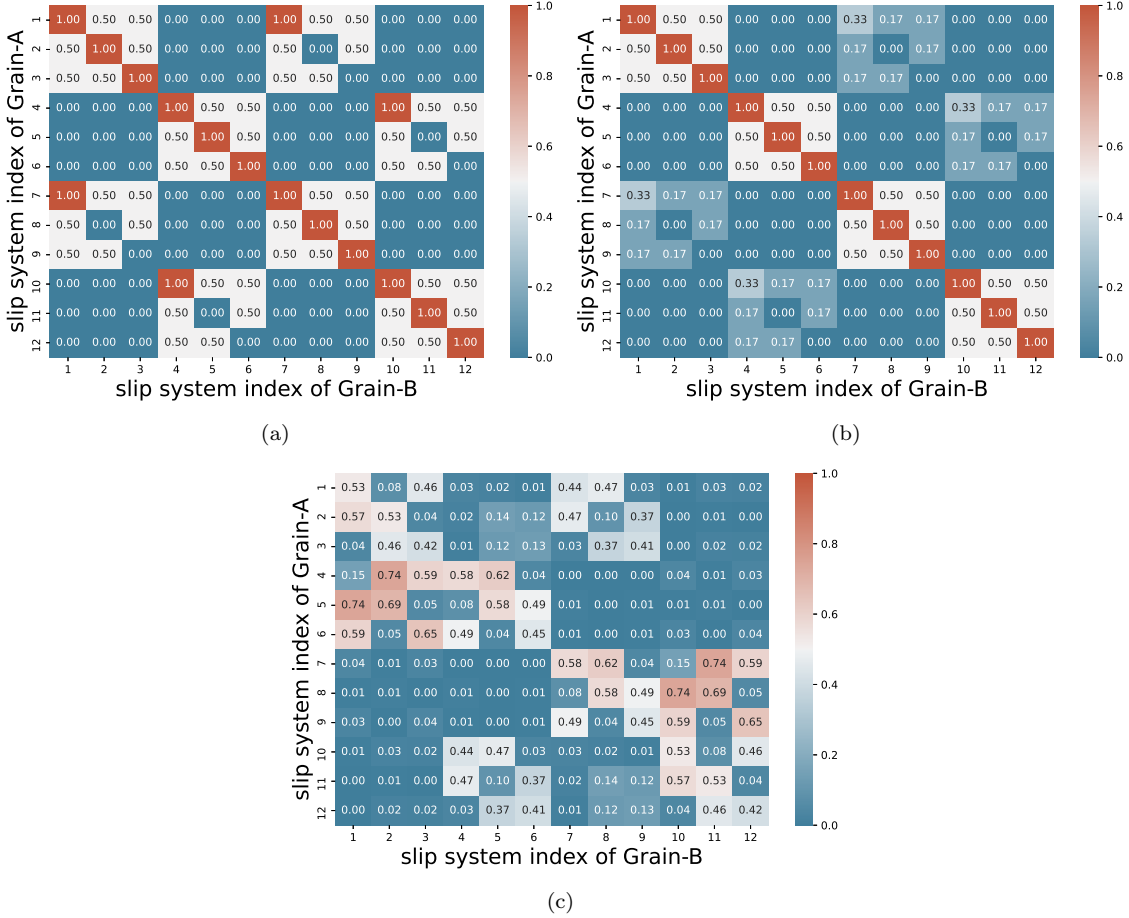
Figure 3: Interaction matrix for transfer of dislocations across a GB based on (a) criterion equation 31 with misorientation angle of $0°$, (b) criterion equation 32 with misorientation angle of $0°$ and (c) criterion equation 32 with misorientation angle of $50°$. Statistical data visualization tool Seaborn [37] is used to plot these data as heat-map.

for slip transmission of 12 possible fcc slip systems for a bi-crystal in which both grains are aligned (i.e. zero misorientation). The slip plane normal and slip direction corresponding to the slip system index are given in Table 3 of Appendix A. For this case in which the two grains are perfectly aligned, each of the slip systems in both grains are also perfectly aligned with their corresponding system. Thus, it is expected that dislocations should continue gliding precisely along the same slip system after crossing the GB. However, it can be seen from Figure 3(a) that this particular interaction matrix (equation 31) fails to provide an unique direction of slip transfer. Specifically, ideal slip transfer is indicated for four cases off the diagonal of the matrix. Therefore, we propose a new criterion which fulfills this basic requirement in the limit of perfect alignment and is defined as

$$M_{\alpha\beta}^{\mathrm{mod}} = (|\mathbf{l}_A^\alpha \cdot \mathbf{l}_B^\beta|)(\mathbf{s}_A^\alpha \cdot \mathbf{s}_B^\beta)(\mathbf{n}_A^\alpha \cdot \mathbf{n}_B^\beta). \tag{32}$$

8

This criterion incorporates the geometric features of both the slip systems in the two grains comprising the GB as well as GB itself.

Figures 3(b) and (c) shows coefficient values in the new interaction matrix $M_{\alpha\beta}^{mod}$ for two different grain misorientations. Similar to Figure 3(a) for the interaction matrix of equation 31, Figure 3(b) highlights the case of zero misorientation between the two grains. Figure 3(c) presents a new interaction matrix for a bi-crystal with Euler angles of (30,0,0) for Grain A and (-20,0,0) for Grain B respectively according to Bunge convention. This is representative of a $50°$ misorientation between the two grains with respect to the Z-axis, which is along the $[0,0,1]$ direction. With this revised geometric criterion, for zero misorientation, Figure 3(b) now shows what one would expect for the case in which all slip systems are perfectly aligned. Now, in this case, dislocations will continue to glide in the same outgoing slip system as incoming slip system, and this is now a unique solution. When there is finite misorientation e.g, Figure 3(c), the interaction matrix can have the largest value for each row in an off-diagonal position. The interaction matrix with off-diagonal dominant terms signifies that slip system index of the incoming dislocations ('in') is different than the outgoing dislocations ('out'). For example, if we explore row-7 of Figure 3(c) we can conclude that if there is an accumulation of dislocation at the GB on slip system-7 of Grain A then it is more likely that most of those dislocations will propagate to slip system-11 of Grain B. We will see an example problem using this orientation in Section 3.2 on how dislocation gets transferred between different slip systems at the GB according to this interaction matrix. In the present work, for each slip system of the incoming dislocations there will be exactly one slip system for outgoing dislocation. In a future study, we plan to incorporate transfer from one to many slip systems based on some critical value of the components of the interaction matrix.

Once the direction of slip transfer from incoming ('in') dislocations to outgoing ('out') dislocations at the GB is identified, the transferred flux at the GB from slip system α of Grain A to β of Grain B is expressed as,

$$f_{G_B(\text{in})}^{\beta} = f_{G_A(\text{out})}^{\alpha} = \begin{cases} \rho_{G_A}^{\alpha} \mathbf{v}_{G_A}^{\alpha} \cdot \mathbf{n}_\Gamma & \text{when} \quad \begin{cases} \rho_{G_A}^{\alpha} > \rho_{\text{crt}} \\ \tau_{G_A}^{\alpha} > \tau_{\text{crt}} \end{cases} \\ 0 & \text{otherwise} \end{cases} \tag{33}$$

where $\rho_{G_A}^{\alpha}, \mathbf{v}_{G_A}^{\alpha}$ are dislocation density and velocity vector respectively for α slip system of Grain A. $\mathbf{n}_\Gamma$ is the unit normal to the GB between Grain A and Grain B and pointing away from Grain A. ρ_{crt} represents the critical dislocation density beyond which dislocation transfer across the GB happens. ρ_{crt} assumes the magnitude of the initial dislocation density when there is no misorientation between two grains. Also at zero misorientation, the interaction matrix becomes diagonal and the maximum magnitude at the diagonal becomes 1.00. Hence the following linear form of ρ_{crt} is used in the present study,

$$\rho_{\text{crt}} = \rho_0 + (\rho_{\text{crt}}^* - \rho_0) \left(1 - \max\left[M_{\alpha\beta}^{\text{mod}} : \beta = 1, N_{\text{slip}}\right]\right) \tag{34}$$

ρ_{crt}^* and τ_{crt} are material parameters. For each slip system in Grain A (α), the corresponding β slip system in Grain B is determined from the interaction matrix. It should also be noted that the slip transfer across the GB occurs only when $\mathbf{v}_{G1}^{\alpha} \cdot \mathbf{n}_{G_A - G_B}$ assumes a positive value. Figure 4 shows the seamless transfer of dislocation across a fictitious GB with zero misorientation between two grains. It can be seen that due to the zero misorientation there is no accumulation of dislocation at the GB. The figure 4(b) shows the positive and negative edge dislocation density of slip system 1 only among all other active slip systems.

2.4 Numerical implementation of the model into MOOSE

The model is implemented with an implicit time integration scheme within the MOOSE. The main equation that need to be time integrated within the crystal plasticity model is equation 4. During the time increment from (t) to (t+Δt) the updated $\mathbf{F}_\text{p}$ can be expressed as:

$$\mathbf{F}_\text{p}(t + \Delta t) = \left(\mathbb{I} + \sum_{\alpha=1}^{N_s} \Delta t \dot{\gamma}^{\alpha} \mathbf{s}_0^{\alpha} \otimes \mathbf{n}_0^{\alpha}\right) \mathbf{F}^p(t) \tag{35}$$
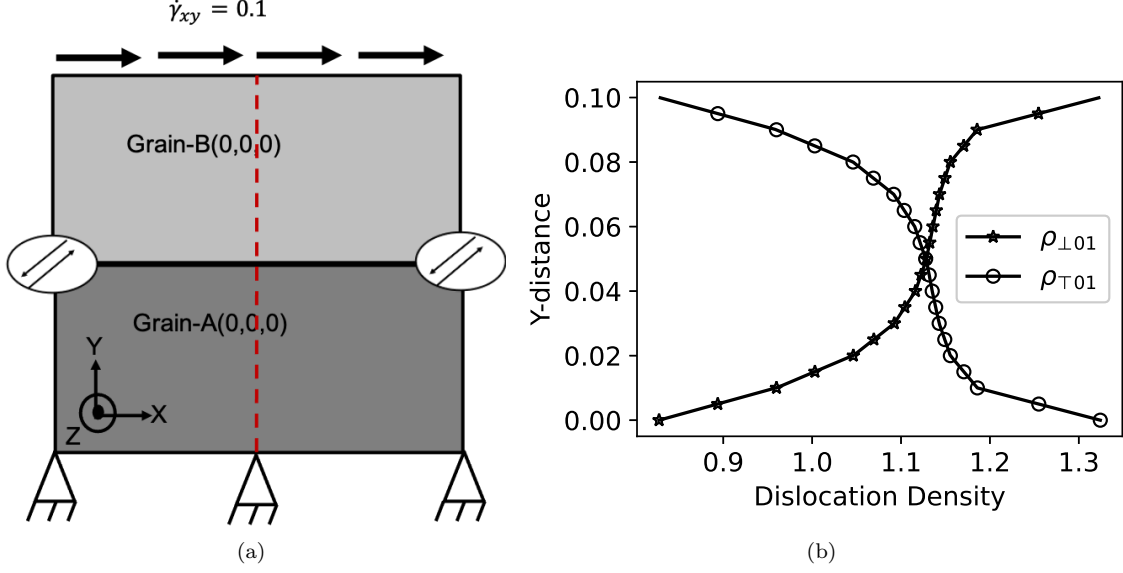
9

Figure 4: Dislocation transfer across a GB when two grains are perfectly aligned. (a) The problem set-up. (b) Spatial distribution of dislocation density along the vertical line through the middle of the sample (the red dashed line). The magnitude of the dislocation density is normalized to initial dislocation density $\rho_0 = 1.0 \times 10^5\, mm^{-2}$.

With this updated $\mathbf{F}_{\mathrm{p}}(t + \Delta t)$, the incremented second Piola-Kirchhoff stress can be written as,

$$\begin{aligned}
\mathbf{S}(t + \Delta t) &= \mathbb{C} : \mathbf{E}_{\mathrm{e}}(t + \Delta t) \\
&= \frac{1}{2}\mathbb{C} : \left(\mathbf{F}_{\mathrm{e}}^{T}(t + \Delta t)\mathbf{F}_{\mathrm{e}}(t + \Delta t) - \mathbf{I}\right) \\
&= \frac{1}{2}\mathbb{C} : \left(\mathbf{F}_{\mathrm{p}}^{-T}(t + \Delta t)\mathbf{F}^{T}(t + \Delta t)\mathbf{F}(t + \Delta t)\mathbf{F}_{\mathrm{p}}^{-1}(t + \Delta t) - \mathbf{I}\right) \\
&\approx \frac{1}{2}\mathbb{C} : [\mathbf{A}(t + \Delta t) - \mathbb{I}] - \sum_{\alpha} \Delta t \dot{\gamma}(\mathbf{S}(t + \Delta t), \tau_b^{\alpha}(t + \Delta t), \tau_{cr}^{\alpha}(t + \Delta t))\mathbf{B}^{\alpha}
\end{aligned}$$

(36)

where

$$\begin{aligned}
\mathbf{A}(t + \Delta t) &\overset{\mathrm{def}}{=} \mathbf{F}^{p-T}(t)\mathbf{F}^{T}(t + \Delta t)\mathbf{F}(t + \Delta t)\mathbf{F}^{p-1}(t) \\
\mathbf{B}^{\alpha} &\overset{\mathrm{def}}{=} \frac{1}{2}\mathbb{C} : [\mathbf{A}(t + \Delta t)\mathbf{S}_0^{\alpha} + \mathbf{S}_0^{\alpha\,T}\mathbf{A}(t + \Delta t)]
\end{aligned}$$

(37)

The nonlinear equation 36 is solved iteratively using Newton-Raphson solver for second Piola-Kirchhoff stress. The i'th iteration can be written as,

$$\mathbf{S}^{i+1}(t + \Delta t) = \mathbf{S}^{i}(t + \Delta t) - \mathbb{J}^{-1} : \mathbb{R}^{i}$$

(38)

where $\mathbb{R}$ is the residual and $\mathbb{J}$ is the Jacobian. The residual $\mathbb{R}$ is computed on the second Piola-Kirchhoff stress and can be expressed as,

$$\mathbb{R}^{i} = \mathbf{S}^{i}(t + \Delta t) - \mathbb{C} : \mathbf{E}_{\mathrm{e}}(t + \Delta t)$$

(39)

Thus the Jacobian becomes,

$$\mathbb{J} = \frac{\partial \mathbb{R}^{i}}{\partial \mathbf{S}^{i}} = \mathbb{I} - \left[\mathbb{C} : \frac{\partial \mathbf{E}_{\mathrm{e}}}{\partial \mathbf{F}_{\mathrm{e}}} \frac{\partial \mathbf{F}_{\mathrm{e}}}{\partial \mathbf{F}_{\mathrm{p}}^{-1}} \frac{\partial \mathbf{F}_{\mathrm{p}}^{-1}}{\partial \mathbf{S}}\right]$$

(40)

Figure 5 shows the flowchart for the stress update loop.

For numerical implementation of the dislocation transport, the equation 28 is converted to it's weak form. The corresponding residual can be written as

$$\mathbb{R}^{i} = \left(\psi_i, \frac{\partial \rho_h}{\partial t}\right) - (\nabla\psi_i, \mathbf{v}\rho) + \langle\psi_i, \mathbf{v}\rho.\mathbf{n}\rangle - (\psi_i s)$$
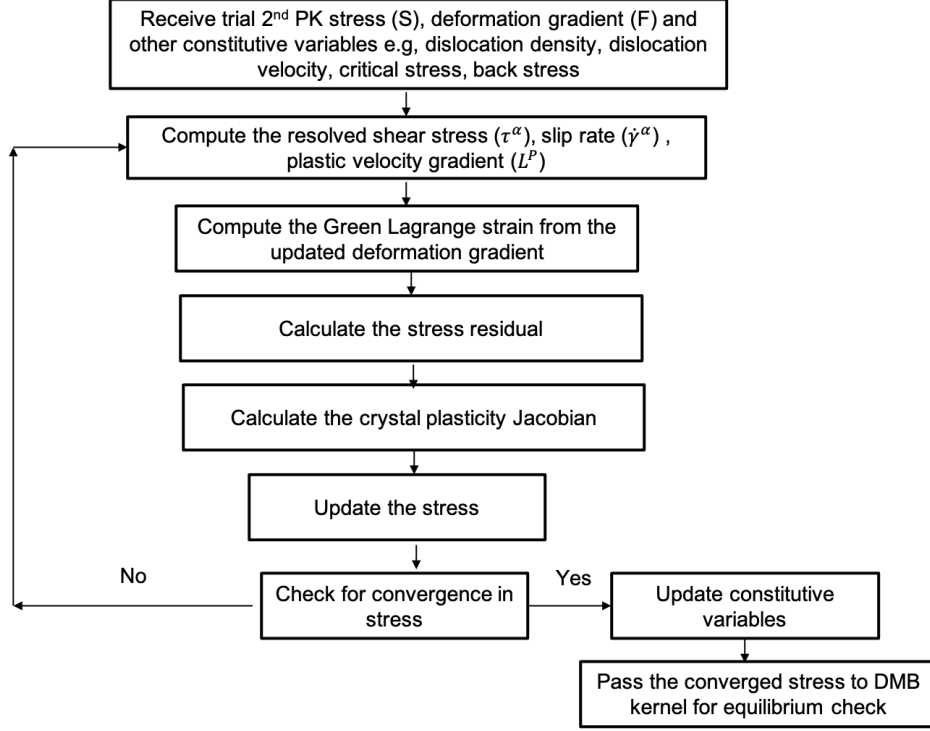
(41)

10

Figure 5: Flow chart for the stress update loop within the DMB module.

where ψ_i is the test function and ρ_h is the trial solution. The terms within first bracket ($\bullet$) are volume integrated and terms within the angular bracket $\langle \bullet \rangle$ are surface integrated. The numerical solution of hyperbolic PDEs, e.g. the above mentioned advection equation, are prone to show oscillation in their solution. Some kind of numerical stabilization is needed to eliminate this oscillation. In the present study to eliminate this spurious oscillation mass lumping is used for the time derivative term i.e, the first term in the equation 41 and the 'upwind' scheme is used for the stabilization purpose of the advection term [38]. Correction due to the upwind scheme only effects the second term in equation 41. To construct the modified residual, first the upwind and downwind nodes are identified in an element. For this purpose, first we compute

$$\widetilde{\mathbb{R}}^i = -\left(\nabla \psi_i, \mathbf{v}\right) \tag{42}$$

if $\widetilde{\mathbb{R}}^i > 0$ then it signifies that the corresponding node is an 'upwind' node. The residual of the corresponding node is set to,

$$\mathbb{R}^i = \widetilde{\mathbb{R}}^i \rho_i \tag{43}$$

where ρ_i is the dislocation density at node i. Then the total outflow of density from all upwind nodes are computed,

$$M_{out} = \sum_{\text{upwind nodes}} \widetilde{\mathbb{R}}^i \rho_i \tag{44}$$

where M_{out} is the total outflow from the upwind nodes. To conserve the quantity the residual of the downwind nodes are defined as,

$$\mathbb{R}^i = \widetilde{\mathbb{R}}^i M_{out}/M_{in} \tag{45}$$

where M_{in} is defined as,

$$M_{in} = -\sum_{\text{downwind nodes}} \widetilde{\mathbb{R}}^i \tag{46}$$

3 Simulation results and discussion

We apply our DiscoFlux model with the new GB transport theory implemented into MOOSE [17] to numerical test problems in order to assess the implementation. Specifically, we have developed two

11

Parameter	value	Unit	Reference
ρ_0	1.0×10^5	mm^{-2}	[10]
C_{11}	169.0	GPa	[10]
C_{12}	121.0	GPa	[10]
C_{44}	75.3	GPa	[10]
c_{multi}	8.96×10^{-5}	-	-
c_{trap}	3.0×10^{-3}	-	-
c_{m-ann}	0.5	-	-
$c_{imm-ann}$	0.5	-	-
ρ_{crt}^*	$2.2\rho_0$	mm^{-2}	-
τ_{crt}	50	MPa	-
ω	8.0×10^{11}	s^{-1}	[10]
τ_0	10	MPa	[10]
c_1	0.25	-	-
q_1	0.33	-	[10]
q_2	1.63	-	[10]
g_0	0.87	-	[10]
b	2.56×10^{-7}	mm	[39]
B_0	3.0×10^{-11}	MPa-s	[10]

Table 2: Values of the material parameters used in this study.

benchmark problems that compare the simulated deformation response of single crystal and bi-crystal configurations utilizing the new features. In the single crystal benchmark problems there are no grain boundaries, and therefore, the grain boundary dislocation flux model is not invoked. For the bi-crystal and polycrystal benchmark problems, dislocation transport both within the grain and across the grain boundary are present. The material parameters used for all of the benchmark simulations are specified in table 2. These values are largely taken from previous work [10], and those that are not are either material parameters or were simply specified by using reasonable approximations for metals, e.g., copper. In other words, the material model parameters were selected to be approximately representative of copper deformation behavior, but we have not performed any detailed calibration to ensure that they are in fact a detailed representation of any specific material. We note that the primary goal of this work is not identification of the optimal parameter set to represent any actual material. Rather we use reasonable parameter values to demonstrate and assess the new features of the model in a systematic way.

3.1 A single crystal sample under shear loading

DiscoFlux was used to simulate a single crystal under shear loading, and to compute the evolution of several of state variables under these conditions. A rectangular domain of dimension $100\mu m \times 100\mu m \times 50\mu m$ was used for the simulation, and was discretized into 500 regular eight-noded linear Hexahedral elements. The sample was continuously deformed by applying a displacement controlled shear strain ($\dot{\gamma} = 0.1s^{-1}$) at the top surface as shown in figure 6(a). The bottom surface was restrained against any displacement. A free flow boundary condition was applied on the left, right, front, and back surfaces to allow for free flux of dislocations across those surfaces. The free-flow boundary condition is imposed by specifying the boundary term in the weak form of dislocation transport equation 28 i.e., the third term in the residual construction in equation 41. The flux through the external surface can be quantified as,

$$\text{Flux} = \rho\mathbf{v} \cdot \mathbf{n} \tag{47}$$

whether the flux normal to the surface is inflow or outflow is determined based on the sign of $\mathbf{v} \cdot \mathbf{n}$.

Figure 6(b) compares the evolution of the volume-averaged stress with respect to volume-averaged strain when using the local crystal plasticity model (CP-Local) with that obtained when using DiscoFlux with active dislocation transport (CP-DiscoFlux). The difference between these two models is that 'CP-Local' does not include any non-local evolution of the dislocation density field via the spatial dislocation transport mechanism. For CP-Local, the dislocation density field evolves according to equation 12, while for CP-DiscoFlux the dislocation density evolves due to the local evolution (i.e., according to equation
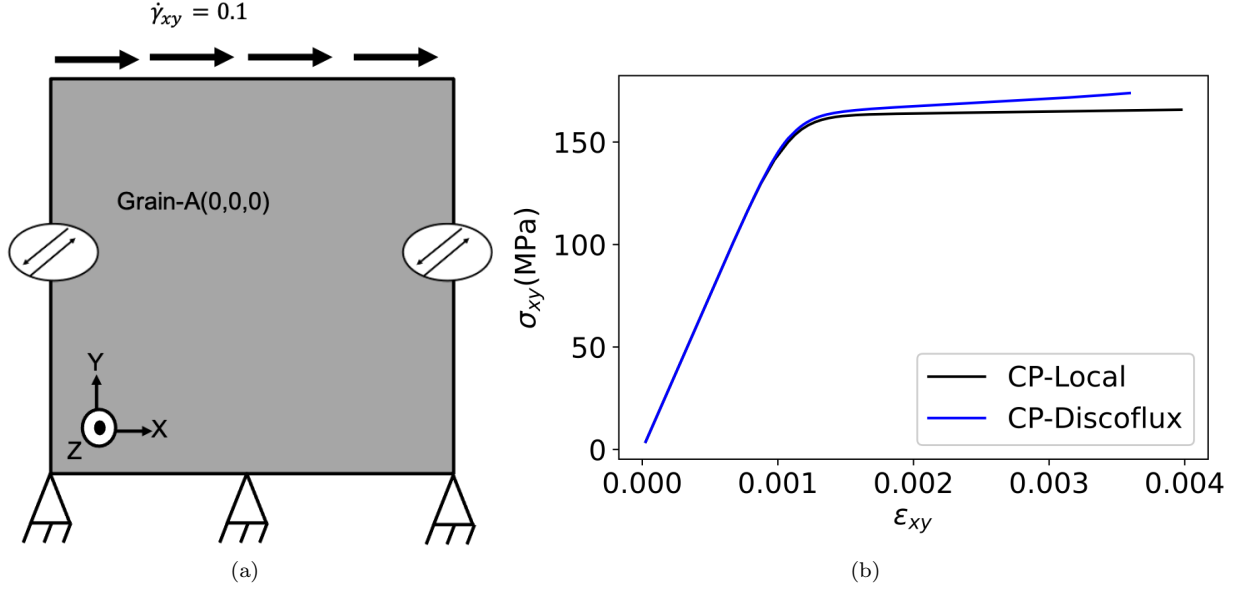
Figure 6: (a) Simulation set-up for single crystal shear test. (b) Evolution of the stress (σ_{xy}) with respect to the strain (ϵ_{xy}) under shear loading in a single crystal.

12), as well as due to the physical transport of dislocations as described in section 2.3. As can be seen from the evolution of the stress, incorporation of dislocation transport (CP-DiscoFlux) within the model leads to the development of GNDs which in turn increases the effective hardening in comparison to that resulting from the CP-Local model.
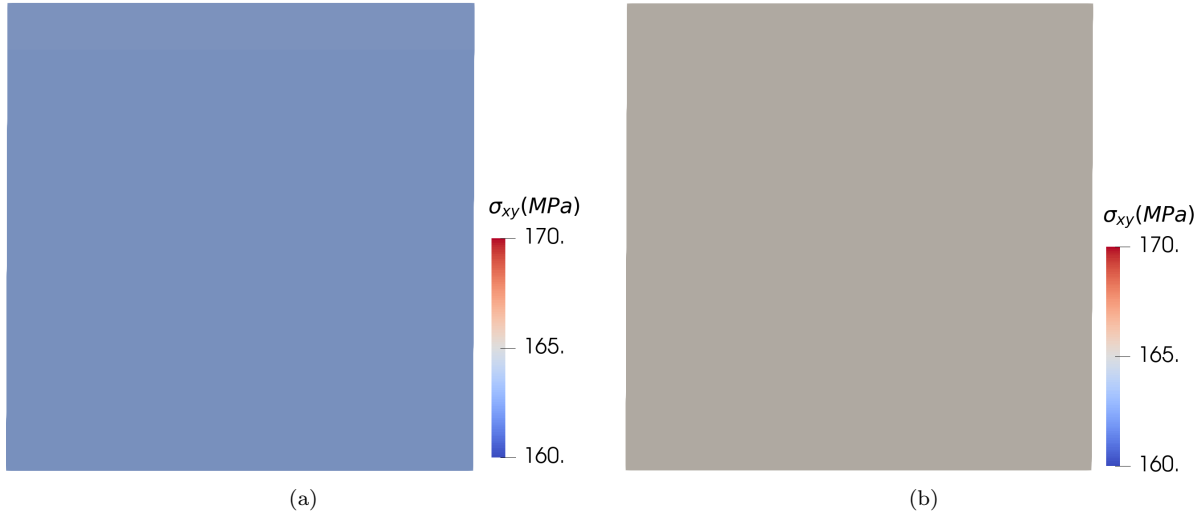
Figure 7: Spatial distribution of the Stress (σ_{xy}) under shear loading in a single-crystal using (a) local crystal plasticity model (CP-Local) and (b)'DiscoFlux' model (CP-DiscoFlux). The figure correspond to the macroscopic volume average strain of $\epsilon_{xy} = 0.003$.

The extra hardening leads to different stress states of the material at the same magnitude of average strain as shown in figure 7 for $\epsilon_{xy} = 0.003$. Both models predict a uniform stress distribution, as is expected for this problem. The increased magnitude of stress in CP-DiscoFlux is due to the back stress and hence the material hardening developed by the dislocation polarity. The extra hardening of the material can be attributed to the fact that due to the transport of dislocations within the grain, the

dislocations, both edge and screw, of opposite character glide in opposite directions (see equation 29). This leads to the development of net polarity of dislocation near the impermeable boundaries.
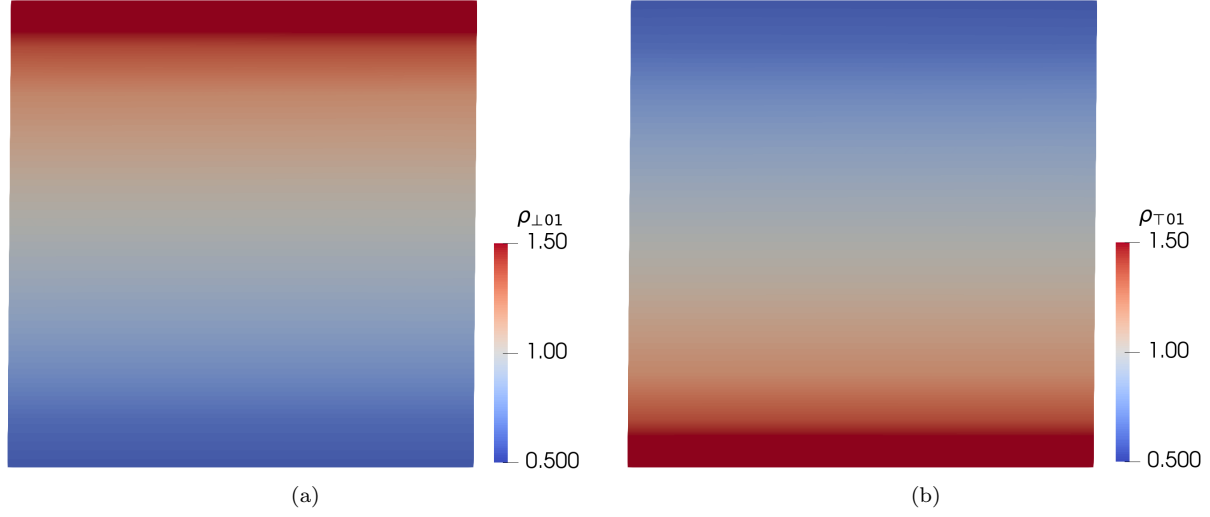

(a)

(b)

Figure 8: Field distribution of the edge dislocation density (a) $\rho_{\perp 01}$ and (b) $\rho_{\top 01}$ on slip system 1 under shear loading in a single crystal using the 'DiscoFlux' model. The magnitude of the dislocation density is normalized to initial dislocation density $\rho_0 = 1.0 \times 10^5 \, mm^{-2}$

Figure 8 shows one such distribution for the edge dislocation density on slip system 1 at a macroscopic strain of $\epsilon_{xy} = 0.003$. Dislocations of positive character have moved towards the top of the domain (a), while dislocations of negative character have moved in the opposite direction (b). This effective segregation of the dislocation field is also reported for Discrete Dislocation Dynamics simulations in [40].

(a)

(b)
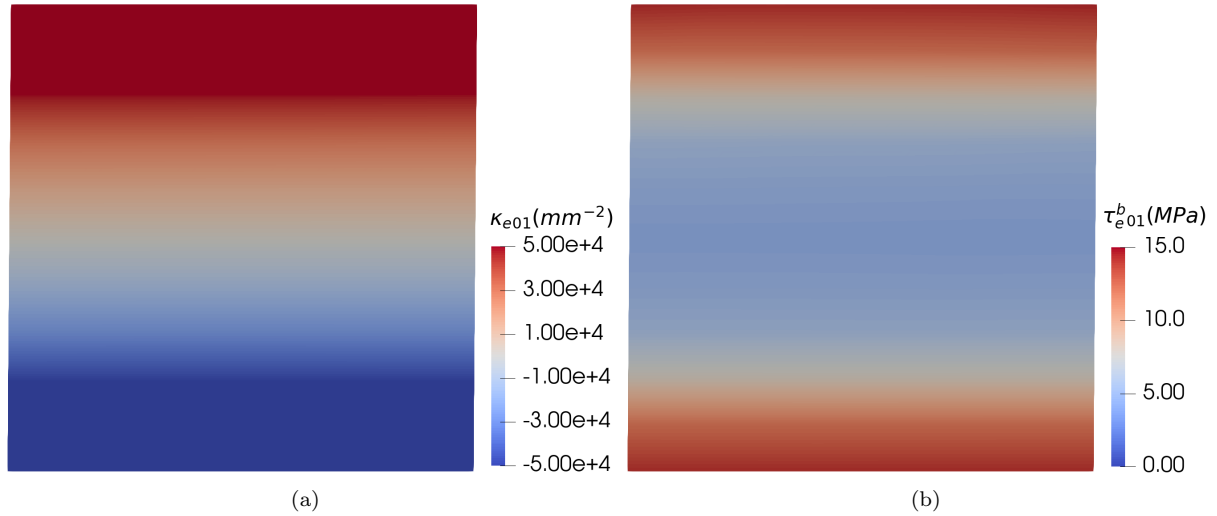
Figure 9: Spatial distribution of (a) dislocation polarity κ^e_{01} and (b) back stress τ^b_{01} on slip system 1 under shear loading in a single crystal using 'DiscoFlux' model.

The corresponding spatial distribution of dislocation polarity for edge dislocations on the first slip system is shown in figure 9(a). The net dislocation polarity is a measure of the GND density in the material. Presence of these GNDs give rise to the internal stress that is quantified in the form of a back stress which is proportional to gradients of κ^e. The associated back stress field within the material is shown in figure 9(b). We note that owing to the free flow boundary condition for dislocation transport on the left, right, front, and back there is no accumulation or depletion of dislocation density along these

14

boundaries. Because this test problem comprises a single crystal, the domain does not include any grain boundary interfaces and therefore the dislocation transfer model discussed in section 2.3.2 is inactive.

3.2   A bi-crystal sample under shear loading

In this section we analyse the results for simulations of a bi-crystal test problem under various model assumptions. Figure 10(a) shows the problem set-up for the bi-crystal. The overall dimension of the sample is 100μm $\times 100\mu$m $\times 10\mu$m. The domain is split equally along y-axis to create two grains. The orientation of the bottom grain (Grain-A) and the top grain (Grain-B) are (30,0,0) and (-20°,0,0) respectively, based on the Bunge [41] rotation convention. Similar to the previous case shown for a single crystal, a fixed displacement boundary condition is applied to the bottom surface of the specimen, and the top surface is deformed at constant shear strain rate of $\dot{\epsilon} = 0.1s^{-1}$. The whole domain is discretized using 200 regular eight-node hexahedron elements. A free flow boundary condition for dislocation transport is applied at the left, right, front and back surfaces.
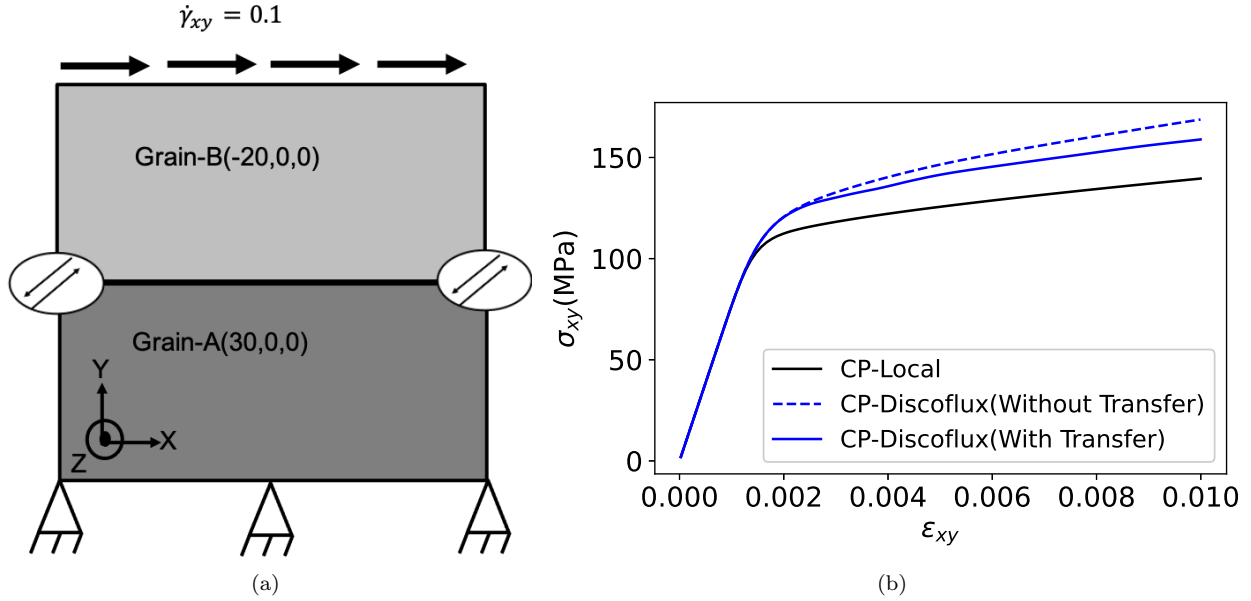

Figure 10: (a) Simulation set-up for a bi-crystal under shear loading. (b) Evolution of the stress (σ_{xy}) with respect to the strain (ϵ_{xy}) under shear loading in a bi-crystal.

Figure 10(b) shows the volume averaged stress-strain response of the specimen for CP-Local and two cases of CP-DiscoFlux, excluding and including the transfer of flux of dislocations across the GB, labeled as CP-DiscoFlux(Without Transfer)) and CP-DiscoFlux(with transfer), respectively. CP-DiscoFlux (both blue curves) exhibits more hardening behavior than the CP-Local model, because of the backstress associated with the pileup of GNDs at the GB. This hardening is slightly reduced for the case where there is finite transmission of dislocation density across the grain boundary (w/ Tx, solid blue curve) in comparison to the case with zero dislocation transmission (blue dashed curve). It can be seen that dislocation transport not only gives rise to additional material hardening in comparison to the CP-Local in both the two cases of the CP-DiscoFlux, but there is also additional hardening in comparison to the CP-DiscoFlux results shown for the previous single crystal simulations (figure 6(b)). The reason for this extra hardening can be attributed to the presence of the grain boundary. The grain boundary prevents the free glide of dislocations resulting in the accumulation or depletion of dislocation density at the grain boundary. It can also be seen that material softens when dislocation transfer across the grain boundary is considered compared to when it is not. This is due to the fact that, as dislocations get transferred across the grain boundary to the appropriate slip system, those dislocation further contributes to the plastic dissipation of the energy based on the local stress state of the material. This in turn contributes in the softening of the material. Figure 11 shows the spatial distribution of the edge positive and edge negative dislocation in the specimen for 7th slip system at the macroscopic strain of $\epsilon_{xy} = 0.005$. In comparison to the single crystal simulation, the grain boundary in the bi-crystal serves as a barrier for free movement
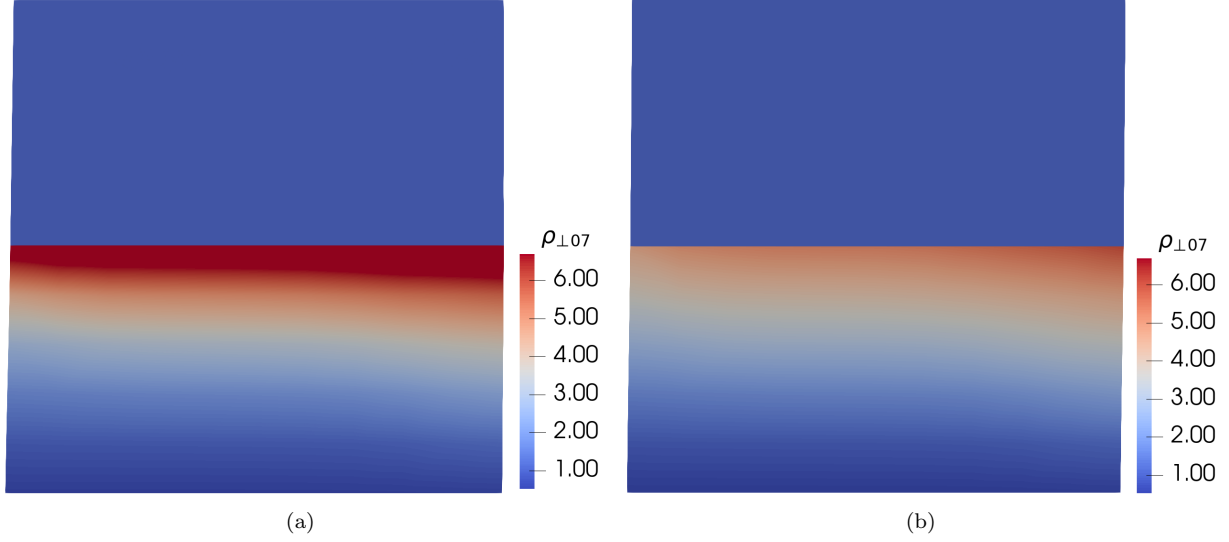
15

Figure 11: Spatial distribution of the dislocation density (a) $\rho_{\perp 07}$ and (b) $\rho_{\top 07}$ on 7'th slip system under shear loading in a bi-crystal using 'DiscoFlux' model. Magnitude of the dislocation density is normalized to initial dislocation density $\rho_0 = 1.0 \times 10^5 \, mm^{-2}$

of dislocation. This results in the accumulation/depletion of dislocation near the grain boundary. The asymmetric distribution of dislocation of opposite polarity gives rise to the development of net polarity of dislocation near the grain boundary. To understand the effect of the dislocation transfer across the
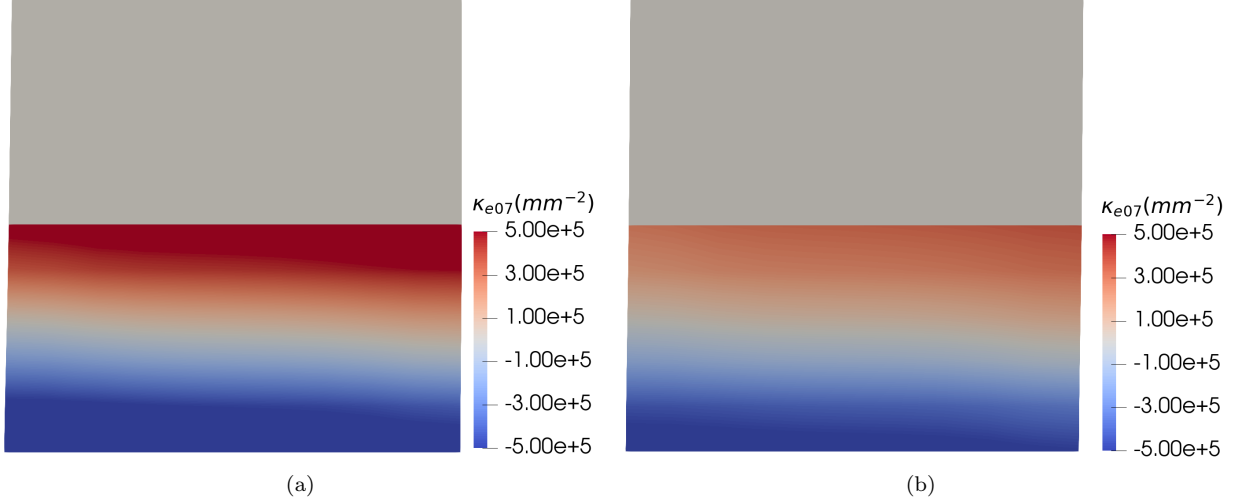
Figure 12: Spatial distribution of dislocation polarity κ_{07}^e (a) without and (b) with the dislocation transfer across the GB on $7'th$ slip system under shear loading in a bi-crystal using 'DiscoFlux' model.

GB, figure 12 shows the spatial distribution of dislocation polarity κ_{07}^e when dislocation transfer across the grain boundary is not considered versus when it is considered. It can seen from figure 12(a) and figure 12(b) that due to the incorporation of the dislocation transfer across GB in the second case, the GND accumulation at the GB is significantly lower. Due to accumulation of GNDs at the GB, there is significant difference in the development of the back stress. Figure 13 shows the spatial distribution of back stress on 7'th slip system. It can be seen that development of back stress near the outer boundary at the bottom is very similar when dislocation transfer across GB is considered versus when it is not.
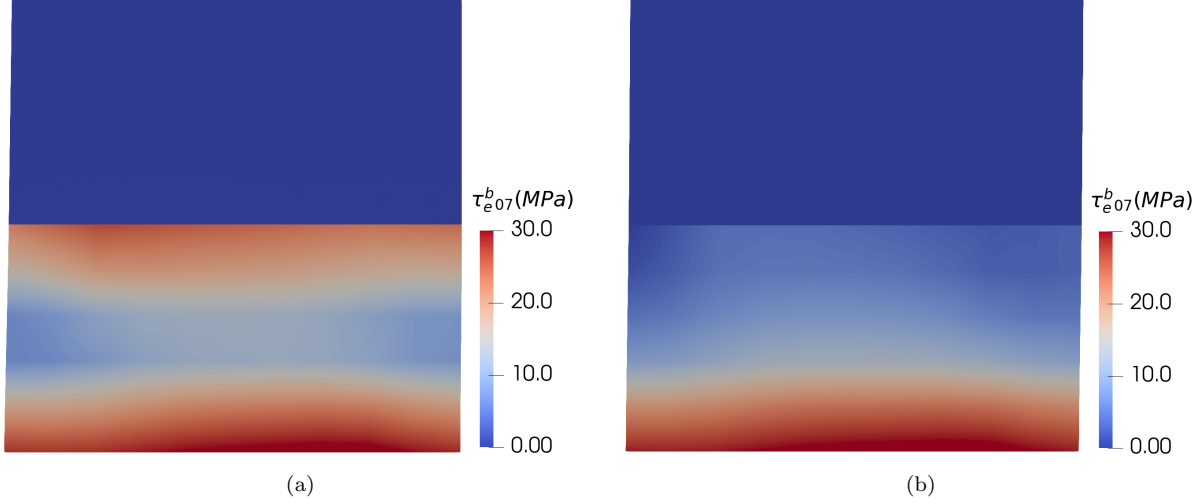
16

Figure 13: Spatial distribution of back stress τ_{07}^b (a) without and (b) with the dislocation transfer across the GB on $7'th$ slip system under shear loading in a bi-crystal using 'DiscoFlux' model.

But there is significant difference at the GB. In fact, when dislocation transfer across the GB is not considered, the GB acts as completely impermeable to dislocation and the magnitude of back stress went as high as 25 MPa. On the other hand when dislocation transfer across the GB is considered, the GB becomes semi-permeable to dislocation. Consequently the back stress drops to 10 MPa near the GB. The field distribution of dislocation polarity and back stress shown in figure 12 and 13 is only for edge dislocation in the 7th slip system. A similar distribution is also there for screw dislocation and for other slip systems as well. Since, the dislocation polarity develops due to the transport of dislocations, to get the dislocation polarity develop the slip system need to be active. As we can see in figure 12 the top grain has both the dislocation polarity as well as back stress almost zero. The reason for this is that the 7'th slip system is not active in the top grain. To understand the dislocation activity at the GB, it is worth to investigate the dislocation transfer between different slip systems at the GB. For this purpose we use the interaction matrix provided in 3(c) to determine the direction of dislocation flow at the GB. From that interaction matrix it can be seen that if there is accumulation of dislocation on slip system 7'th in grain-A at the GB then those dislocations are likely to get transferred on the slip system 11'th of grain-B. Figure 14 shows the spatial distribution of edge positive dislocation density through the middle of the specimen along the y-axis for slip system 7'th and 11'th. It can be seen from figure 14(a and b) that there is significant difference in the distribution of dislocation density in 7'th and 11'th slip system due to he consideration of dislocation transfer across the GB or not. In fact, it can be seen from figure14(b) that when dislocation transfer across the grain boundary is considered, then maximum dislocation accumulation due to dislocation pile up at the GB is $\approx 5e + 05 \ mm^{-2}$. This is not the situation when dislocation transfer across the GB is not considered, rather in this later case dislocation at the grain boundary keep accumulating without any bound. This is because some of the dislocations on 7'th slip system in grain-A get transferred to the 11'th slip system of grain-B. The accumulation of dislocation on the other side of the GB will depend on the resolved shear stress (RSS) on that slip system in grain-B. Since the RSS on slip system 11'th on grain-B is not high enough to move those dislocation away from the grain boundary hence there is large pile-up of dislocation on that side of the GB. But as the more and more dislocations get transferred across the GB onto the 11'th slip system, the internal stress is developed due to high dislocation polarity, this internal stress augments the RSS to spread those dislocations away from the GB. But this internal stress decays drastically away from the GB hence the effect of this internal stress is limited only at the vicinity of the GB. Next, we will investigate another pair of slip system where RSS in the slip system of the grain-B in which the dislocation getting transferred if high enough to move the transferred dislocations away from the GB. Figure 15 shows the distribution of edge positive dislocation density through the middle of the sample along the y-axis for slip system 1'st and 2'nd. From the interaction matrix in figure 3(c) it can be seen that if there is accumulation of dislocation in grain-A on slip system 2'nd near the GB then it is likely that those dislocation will get
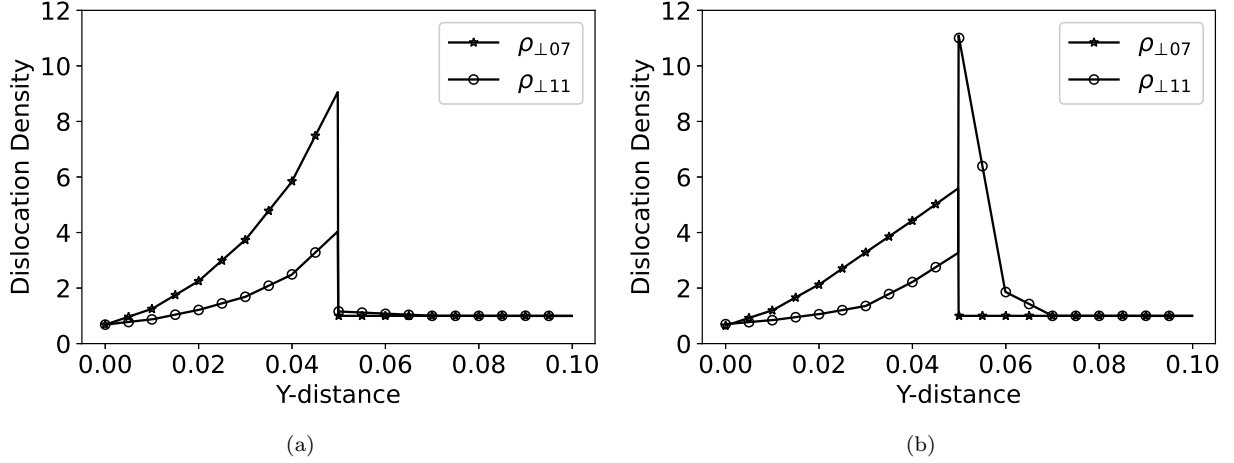
Figure 14: Distribution of dislocation density of 7'th ($\rho_{\perp 07}$) and 11'th ($\rho_{\perp 11}$) slip system along the y-axis through the middle of the sample. 'DiscoFlux' model (a) without and (b) with considering the dislocation transfer across the GB. Magnitude of the dislocation density is normalized to initial dislocation density $\rho_0 = 1.0 \times 10^5 \, mm^{-2}$.
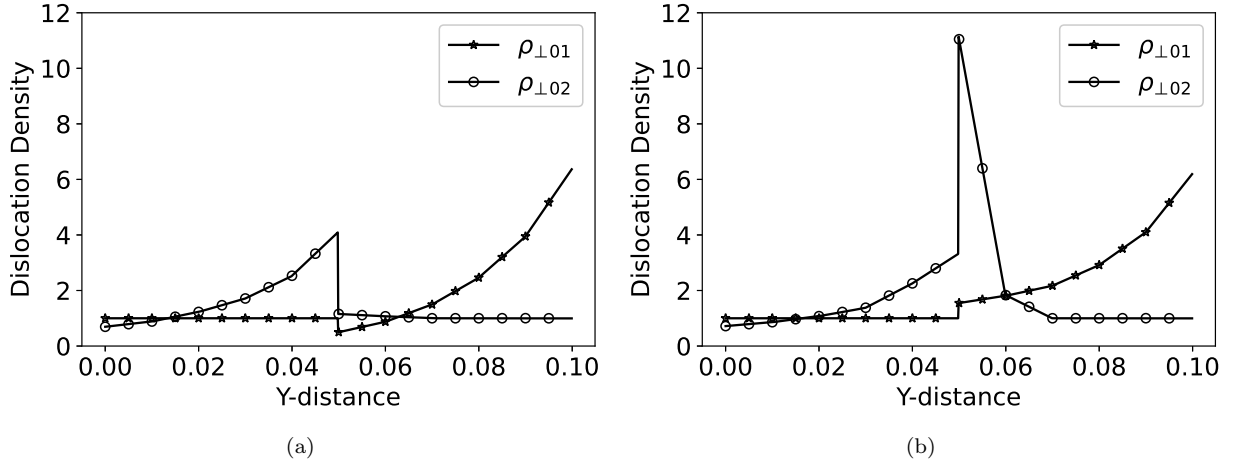

Figure 15: Distribution of dislocation density of 1'st ($\rho_{\perp 01}$) and 2'nd ($\rho_{\perp 02}$) slip system along the y-axis through the middle of the sample. 'DiscoFlux' model (a) without and (b) with considering the dislocation transfer across the GB. Magnitude of the dislocation density is normalized to initial dislocation density $\rho_0 = 1.0 \times 10^5 \, mm^{-2}$.

transferred to slip system 1'st of grain-B. In figure 15 it can be seen that when there is no dislocation transfer across the GB then in grain-A edge positive dislocations in slip system 2'nd get accumulated at the GB and in gran-B edge positive dislocation in slip system 1'st get depleted near the GB. But when dislocation transferred across the GB is considered then dislocation from grain-A in slip system 2'nd gets transferred to the slip system 1'st of grain-B. Due to this, the density of edge positive dislocation in grain-B near the GB is replenished and contrary to being deplete there is accumulation of dislocation. The accumulation is not as strong as we have seen previously in the 11'th slip system because the RSS in the 1'st slip system of grian-B is high enough to move some of the transferred dislocations away from the GB. It is worth to mention that in figure 15(b) there is large accumulation of dislocation in 2'nd slip system in grain-B, this is because there are other slip systems (3'rd and 4'th) in grain-A that is transferring dislocations to the 2'nd slip system in grain-B.

3.3   A poly-crystal sample under shear loading

In the bi-crystal example problem discussed above, the presence of an interface in the form of a grain boundary hinders the free movement of dislocations within the sample. The 'DiscoFlux' model is able to capture the asymmetric distribution of dislocation density due to the physical transport of dislocations within the grain and across the grain boundary. The model is also able to capture the extra material hardening in the form of a back stress.
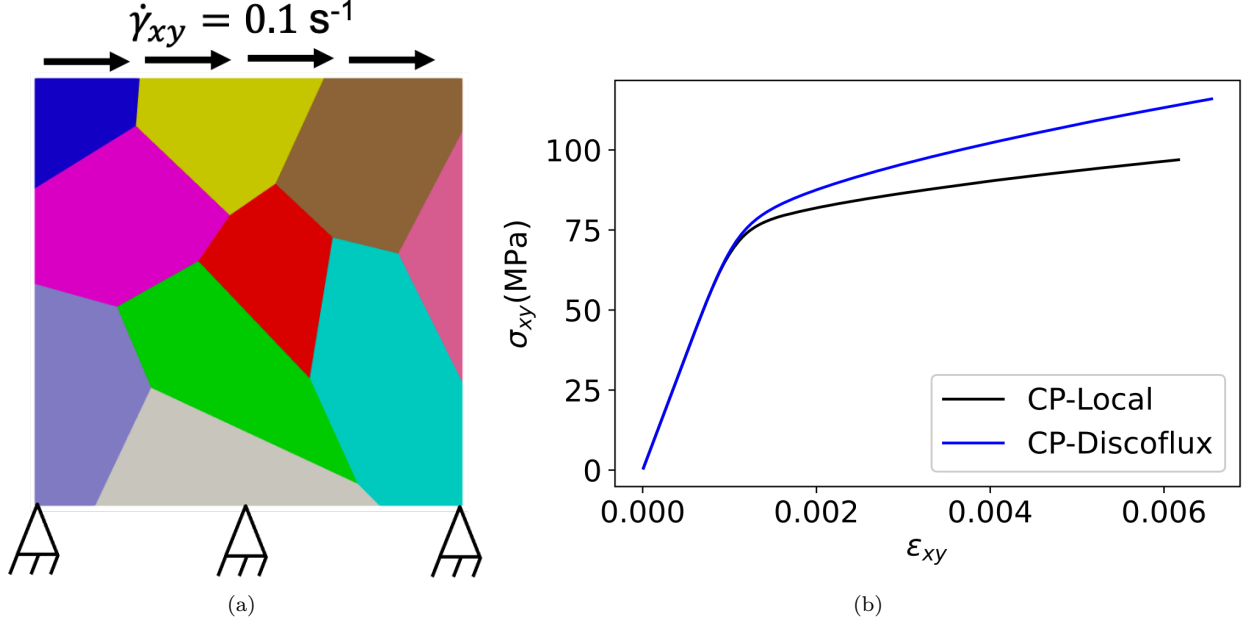

Figure 16: (a) The problem set-up for bi-crystal shear test. (b) Evolution of the stress (σ_{xy}) with respect to the strain (ϵ_{xy}) under shear loading in a polycrystal sample.

Here we report on results for a polycrystalline sample test problem that contains several grains with grain size of $100\mu m$ to $200\mu m$, which is more representative of experimental samples. Figure 16(a) shows the problem setup for a polycrystalline sample. The polycrystalline sample consists of ten grains each with a randomly assigned crystal orientation sampled from $SO(3)$. Again, similar to previous cases, a fixed displacement boundary condition is applied at the bottom surface, and the top surface is deformed at constant shear rate of $\dot{\epsilon} = 0.1s^{-1}$. Contrary to the previous two examples, there is no free-flow boundary condition at any of the external surfaces, which implies an assumption that the external surface of the specimen is in essence a grain boundary. Figure 16(b) shows the volume averaged stress versus strain curve. Both the 'CP-Local' and 'CP-DiscoFlux' models show significant hardening due to the presence of interfaces in the form of grain boundaries. The hardening slope for 'CP-DiscoFlux' is higher in comparison to the 'CP-Local', as expected, due to the development of net dislocation polarity near the grain boundaries and hence the back stress.

Figure 17 shows the spatial distribution of the von-Mises stress in the polycrystal sample for 'CP-Local' and 'CP-DiscoFlux'. Owing to the grain misorientation the polycrystal sample inherently develops a heterogeneous distribution of stress as shown in figure 17(a) with 'CP-Local' model. But the physical transport of dislocation within the grain and across the grain boundary contributes to the extra hardening of the material near grain boundaries which is very evident from the distribution of von-Mises stress in figure 17(b). This excess hardening near grain boundaries and triple junctions can be attributed to the development of back stress due to the net polarity of dislocation at these locations.

Figure 18(a) shows the net-polarity of edge dislocation for 2nd slip system and figure 18(b) shows the development of back-stress due this. Similar inhomogeneity in the distribution of dislocation of opposite character for both edge and screw is present for other slip systems as well.
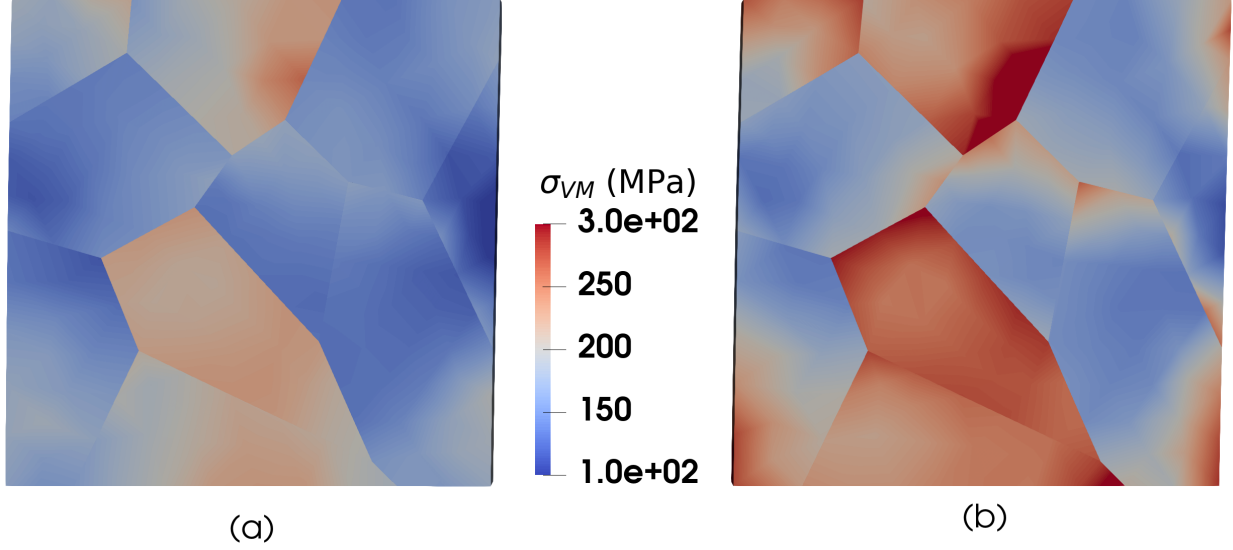
Figure 17: Spatial distribution of the Von-Mises stress under shear loading in a polycrystal using (a) local crystal plasticity model and (b)'DiscoFlux' model.
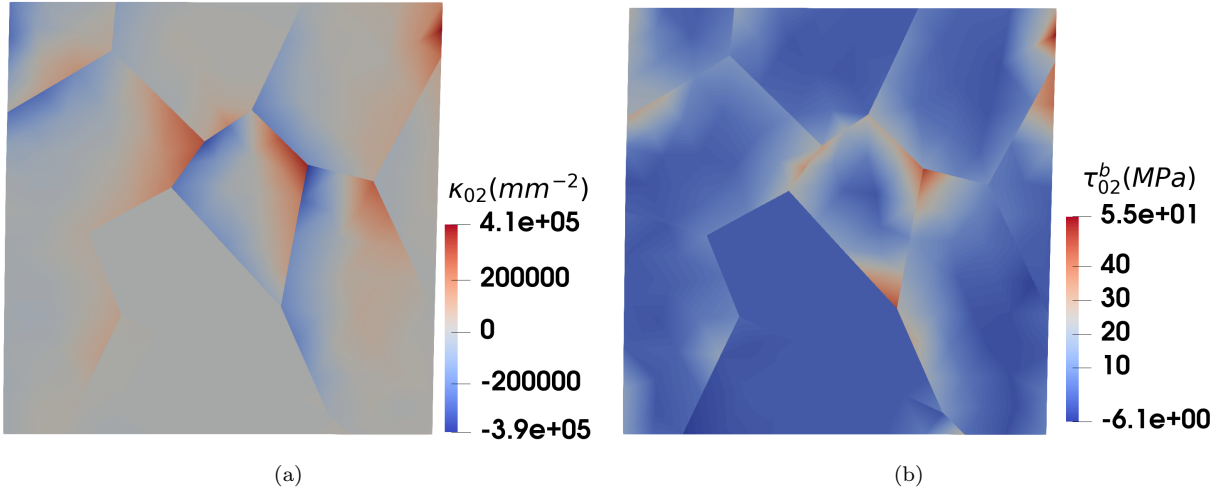

Figure 18: Spatial distribution of (a) dislocation polarity κ_{02}^e and (b) back stress τ_{02}^b on 2'nd slip system under shear loading in a polycrystal using 'DiscoFlux' model.

4   Concluding remarks

In the present work we have presented a dislocation transport based crystal plasticity model where dislocation transport both within and across grains is directly accounted for. To achieve this, we started with an existing dislocation transport based crystal plasticity model developed in LANL called 'Discoflux'. In the existing 'DiscoFlux' model the grain boundaries are treated either as impermeable to dislocation transfer or completely permeable to dislocation transfer. To develop a proper dislocation transfer criterion across the grain boundary, we explore some of the existing models that are based on geometric features. We have outlined the features and limitations of previous criteria and then developed a new criterion that incorporates all the critical requirements of dislocation transfer across the grain boundary. This new criterion is incorporated within the 'DiscoFlux' model. In the present work the modified 'DiscoFlux' model is implemented in the open-source code MOOSE. Implicit time integration scheme is used to integrate the rate equations. We have used this implementation to study some of the benchmark problem

20

of single crystal and bi-crystal to verify the implementation. Then we have used the model to study the material behavior for a polycrystal sample under shear loading. The model is able to successfully predict the extra hardening developed due to the transport of dislocation within and across the grain boundary. The comparison with the local crystal plasticity model shows that the enhanced hardening is more prominent near the high-angle grain boundaries and triple junctions.

Acknowledgement

A   Slip System

In the present work copper has been used as the representation material with fcc crystal structure. The slip system information for fcc material and the index used in the present work is provided in table 3.

Slip System Index	Slip Plane Normal	Slip Direction
1	$[1,1,\bar{1}]$	$[0,1,1]$
2	$[1,1,\bar{1}]$	$[1,0,1]$
3	$[1,1,\bar{1}]$	$[1,\bar{1},0]$
4	$[1,\bar{1},\bar{1}]$	$[0,1,\bar{1}]$
5	$[1,\bar{1},\bar{1}]$	$[1,0,1]$
6	$[1,\bar{1},\bar{1}]$	$[1,1,0]$
7	$[1,\bar{1},1]$	$[0,1,1]$
8	$[1,\bar{1},1]$	$[1,0,\bar{1}]$
9	$[1,\bar{1},1]$	$[1,1,0]$
10	$[1,1,1]$	$[0,1,\bar{1}]$
11	$[1,1,1]$	$[1,0,\bar{1}]$
12	$[1,1,1]$	$[1,\bar{1},0]$

Table 3: Slip system index along with slip plane normal and slip direction used in the present work.

References

[1] T.R. Bieler, R. Alizadeh, M. Peña-Ortega, and J. Llorca. An analysis of (the lack of) slip transfer between near-cube oriented grains in pure Al. *International Journal of Plasticity*, 118:269–290, July 2019.

[2] T.R. Bieler, P. Eisenlohr, C. Zhang, H.J. Phukan, and M.A. Crimp. Grain boundaries and interfaces in slip transfer. *Current Opinion in Solid State and Materials Science*, 18(4):212–226, August 2014.

[3] Josh Kacher, B.P. Eftink, B. Cui, and I.M. Robertson. Dislocation interactions with grain boundaries. *Current Opinion in Solid State and Materials Science*, 18(4):227–243, August 2014.

[4] Josh Kacher and I.M. Robertson. Quasi-four-dimensional analysis of dislocation interactions with grain boundaries in 304 stainless steel. *Acta Materialia*, 60(19):6657–6672, November 2012.

[5] F. Roters, P. Eisenlohr, L. Hantcherli, D.D. Tjahjanto, T.R. Bieler, and D. Raabe. Overview of constitutive laws, kinematics, homogenization and multiscale methods in crystal plasticity finite-element modeling: Theory, experiments, applications. *Acta Materialia*, 58(4):1152–1211, February 2010.

[6] S.R. Kalidindi, C.A. Bronkhorst, and L. Anand. Crystallographic texture evolution in bulk deformation processing of FCC metals. *Journal of the Mechanics and Physics of Solids*, 40(3):537–569, January 1992.

[7] L. Anand and M. Kothari. A computational procedure for rate-independent crystal plasticity. *Journal of the Mechanics and Physics of Solids*, 44(4):525–558, April 1996.

[8] Shahriyar Keshavarz, Somnath Ghosh, Andrew C.E. Reid, and Stephen A. Langer. A non-Schmid crystal plasticity finite element approach to multi-scale modeling of nickel-based superalloys. *Acta Materialia*, 114:106–115, August 2016.

[9] Thao Nguyen, D.J. Luscher, and J.W. Wilkerson. A dislocation-based crystal plasticity framework for dynamic ductile failure of single crystals. *Journal of the Mechanics and Physics of Solids*, 108:1–29, November 2017.

[10] D.J. Luscher, J.R. Mayeur, H.M. Mourad, A. Hunter, and M.A. Kenamond. Coupling continuum dislocation transport with crystal plasticity for application to shock loading conditions. *International Journal of Plasticity*, 76:111–129, January 2016.

[11] Jason R Mayeur, Hashem M Mourad, Darby J Luscher, Abigail Hunter, and Mark A Kenamond. Numerical implementation of a crystal plasticity model with dislocation transport for high strain rate applications. *Modelling and Simulation in Materials Science and Engineering*, 24(4):045013, May 2016.

[12] Sarra Haouala, Javier Segurado, and Javier LLorca. An analysis of the influence of grain size on the strength of FCC polycrystals by means of computational homogenization. *Acta Materialia*, 148:72–85, April 2018.

[13] S. Haouala, R. Alizadeh, T.R. Bieler, J. Segurado, and J. LLorca. Effect of slip transmission at grain boundaries in Al bicrystals. *International Journal of Plasticity*, 126:102600, March 2020.

[14] Doris Kuhlmann-Wilsdorf. Dislocation cells, redundant dislocations and the leds hypothesis. *Scripta Materialia*, 34(4):641–650, February 1996.

[15] J. A. Hurtado and J. Weertman. Non-redundant dislocation density field of a circular bar deformed in torsion and the stress gradient hardening effect. *physica status solidi (a)*, 149(1):173–186, 1995.

[16] Yinguang Piao and Khanh Chau Le. Thermodynamic theory of dislocation/grain boundary interaction. *Continuum Mechanics and Thermodynamics*, 34(3):763–780, May 2022.

[17] Derek Gaston, Chris Newman, Glen Hansen, and Damien Lebrun-Grandié. MOOSE: A parallel computational framework for coupled systems of nonlinear equations. *Nuclear Engineering and Design*, 239(10):1768–1778, October 2009.

[18] PETSc web page. https://petsc.org/, 2023.

[19] Satish Balay, William D. Gropp, Lois Curfman McInnes, and Barry F. Smith. Efficient Management of Parallelism in Object-Oriented Numerical Software Libraries. In Erlend Arge, Are Magnus Bruaset, and Hans Petter Langtangen, editors, *Modern Software Tools for Scientific Computing*, pages 163–202. Birkhäuser Boston, Boston, MA, 1997.

[20] U. F. Kocks, Ali S. Argon, and M. F. Ashby. *Thermodynamics and Kinetics of Slip*. Number v. 19 in Progress in Materials Science. Pergamon Press, Oxford ; New York, 1st ed edition, 1975.

[21] Athanasios Arsenlis and David M. Parks. Modeling the evolution of crystallographic dislocation density in crystal plasticity. *Journal of the Mechanics and Physics of Solids*, 50(9):1979–2009, September 2002.

[22] A.H. Cottrell. The formation of immobile dislocations during slip. *The London, Edinburgh, and Dublin Philosophical Magazine and Journal of Science*, 43(341):645–647, June 1952.

[23] N.A Fleck, M.F Ashby, and J.W Hutchinson. The role of geometrically necessary dislocations in giving material strengthening. *Scripta Materialia*, 48(2):179–183, January 2003.

[24] M. F. Ashby. The deformation of plastically non-homogeneous materials. *The Philosophical Magazine: A Journal of Theoretical Experimental and Applied Physics*, 21(170):399–424, February 1970.

[25] Ryan A. Austin and David L. McDowell. A dislocation-based constitutive model for viscoplastic deformation of fcc metals at very high strain rates. *International Journal of Plasticity*, 27(1):1–24, January 2011.

[26] U.F. Kocks and H. Mecking. Physics and phenomenology of strain hardening: The FCC case. *Progress in Materials Science*, 48(3):171–273, January 2003.

[27] B. Devincre, T. Hoc, and L. Kubin. Dislocation Mean Free Paths and Strain Hardening of Crystals. *Science*, 320(5884):1745–1748, June 2008.

[28] C.J. Bayley, W.A.M. Brekelmans, and M.G.D. Geers. A comparison of dislocation induced back stress formulations in strain gradient crystal plasticity. *International Journal of Solids and Structures*, 43(24):7268–7286, November 2006.

[29] L Evers. Non-local crystal plasticity model with intrinsic SSD and GND effects. *Journal of the Mechanics and Physics of Solids*, 52(10):2379–2401, October 2004.

[30] J.D Livingston and B Chalmers. Multiple slip in bicrystal deformation. *Acta Metallurgica*, 5(6):322–327, June 1957.

[31] Michael D. Sangid, Tawhid Ezaz, Huseyin Sehitoglu, and Ian M. Robertson. Energy of slip transmission and nucleation at grain boundaries. *Acta Materialia*, 59(1):283–296, January 2011.

[32] E. Bayerschen, A. T. McBride, B. D. Reddy, and T. Böhlke. Review on slip transmission criteria in experiments and crystal plasticity models. *Journal of Materials Science*, 51(5):2243–2258, March 2016.

[33] Y. Guo, T.B. Britton, and A.J. Wilkinson. Slip band–grain boundary interactions in commercial-purity titanium. *Acta Materialia*, 76:1–12, September 2014.

[34] J. Luster and M. A. Morris. Compatibility of deformation in two-phase Ti-Al alloys: Dependence on microstructure and orientation relationships. *Metallurgical and Materials Transactions A*, 26(7):1745–1756, July 1995.

[35] Z. Shen, R.H. Wagoner, and W.A.T. Clark. Dislocation pile-up and grain boundary interactions in 304 stainless steel. *Scripta Metallurgica*, 20(6):921–926, June 1986.

[36] Z. Shen, R.H. Wagoner, and W.A.T. Clark. Dislocation and grain boundary interactions in metals. *Acta Metallurgica*, 36(12):3231–3242, December 1988.

[37] Michael Waskom. Seaborn: Statistical data visualization. *Journal of Open Source Software*, 6(60):3021, April 2021.

[38] Vilgeir Dalen. Simplified Finite-Element Models for Reservoir Flow Problems. *Society of Petroleum Engineers Journal*, 19(05):333–343, October 1979.

[39] K. M. Jassby and T. Vreeland. Dislocation Mobility in Pure Copper at 4.2 °K. *Physical Review B*, 8(8):3537–3541, October 1973.

[40] S. Yefimov and E. Van Der Giessen. Multiple slip in a strain-gradient plasticity model motivated by a statistical-mechanics description of dislocations. *International Journal of Solids and Structures*, 42(11-12):3375–3394, June 2005.

[41] H.-J. Bunge. *Texture Analysis in Materials Science: Mathematical Methods*. Elsevier Science, Cambridge, 2014.

[42] James Ahrens, Berk Geveci, and Charles Law. ParaView: An End-User Tool for Large-Data Visualization. In *Visualization Handbook*, pages 717–731. Elsevier, 2005.